High-valence-state manganate(V) $Ba_3Mn_2O_8$ as an efficient anode of a proton-conducting solid oxide steam electrolyzer

Journal:	*Inorganic Chemistry Frontiers*
Manuscript ID	QI-RES-03-2019-000253.R1
Article Type:	Research Article
Date Submitted by the Author:	25-Apr-2019
Complete List of Authors:	Toriumi, Hajime; Hokkaido University Kobayashi, Taisei; Hokkaido University, Graduate School of Chemical Sciences and Engineering Hinokuma, Satoshi; Kumamoto University, Graduate School of Science and Technology Ina, Toshiaki; Japan Synchrotron Radiation Research Institute, Researcg and Utilization Division nakamura, takashi; Tohoku University Amezawa, Koji; Tohoku University, Graduate School of Environmental Studies Zhu, Chunyu; Hokkaido university, divison of applied chemistry Aoki, Yoshitaka; Hokkaido University, Faculty of Engineering Habazaki, Hiroki; Hokkaido University,

ARTICLE

High-valence-state manganate(V) $Ba_3Mn_2O_8$ as an efficient anode of a proton-conducting solid oxide steam electrolyzer

Hajime Toriumi,[a] Taisei Kobayashi, [a] Satoshi Hinokuma,[b] Toshiaki Ina,[c] Takashi Nakamura,[d] Koji Amezawa,[d] Chunyu Zhu,[e] Hiroki Habazaki,[e] Yoshitaka Aoki,[e]*

Received 00th January 20xx,
Accepted 00th January 20xx

DOI: 10.1039/x0xx00000x

Herein, high-valence-state Mn(V) oxide, barium manganate(V) ($Ba_3(MnO_4)_2$), was examined as an anode electrocatalyst of a H^+-conducting solid oxide steam electrolysis cell (H-SOEC). $Ba_3(MnO_4)_2$ comprises C_{3v}-symmetric MnO_4^{3-} oxo-anions with three longer Mn-O1 bonds and one shorter Mn-O2 bond at room temperature. $Ba_3(MnO_4)_2$ caused a conductivity jump by one order of magnitude at approximately 600 °C owing to the antiferromagnetic/paramagnetic phase transition, accompanied with a shape change of the tetrahedral MnO_4^{3-} anions from C_{3v} to T_d symmetry, as confirmed by electrical conductivity measurements and extended X-ray adsorption fine structure at an elevated temperature. Hence, the $Ba_3(MnO_4)_2$ base anode of the H-SOEC exhibited improved performance, with the anode polarization resistances smaller than those of $Sm_{0.5}Sr_{0.5}CoO_3$, a well-known H-SOEC anode material. Impedance analysis in terms of the oxygen and water partial pressure revealed that the superior performance of the $Ba_3(MnO_4)_2$ base anode can be attributed to the extended reaction area. Since abundant unoccupied 3d states of the high-valence-state Mn^{5+} cations are favorable for charge transfer interactions with water electron donors, thereby facilitating water adsorption, the oxygen evolution reaction could occur directly over the electrode surface, and thus the reaction sites were not limited to the gas-electrode-electrolyte triple phase boundary.

Introduction

There has been strong interest in clean and renewable energy sources owing to finite fossil fuel sources, increasing oil price, and environmental concerns. Hydrogen is regarded as a leading candidate fuel, because it releases only H_2O during combustion and it is compatible with high-efficiency fuel systems. Steam reforming of hydrocarbon gas is currently the main way to produce hydrogen, but it still relies on fossil fuel. On the contrary, water electrolysis using electric power generated by renewable energy is attracted as a sustainable hydrogen production method. In particular, steam electrolysis using solid electrolyte cells is promising for efficient hydrogen production, because high heat partly offers the energy for water electrolysis, resulting in favorable kinetics and thermodynamics.[1,2] Conventional solid oxide electrolyzer cells (SOECs) using oxide-ion-conducting electrolytes such as yttria-stabilized zirconia (YSZ) require very high temperatures (typically, >900 °C) of operation because of the poor conductivity of YSZ at lower temperatures, which leads to problems such as reduced cell life, fabrication challenges, and material problems.[2–5]

Proton-conducting perovskite-type oxides, such as $BaZr_{0.8}M_{0.2}O_3$ or $BaCe_{0.8}M_{0.2}O_3$ (where M is, for example, Y, Gd, or Yb), have been reported to have higher ion conductivities than the oxide-ion-conducting oxides based on zirconia between 400 and 700 °C,[6–8] and thus, recently, interest in SOECs using these proton-conducting ceramic electrolytes (H^+-SOECs) has increased, because they allow lower working temperatures.[2,9] However, development of H^+-SOECs is still a challenge owing to various issues that need to be solved, one of which concerns anode reactions. As is the case with alkaline electrolysis,[10] four-electron transfer oxygen evolution reactions (OERs) at the anodes was recognized to involve relatively large overpotentials in comparison to hydrogen evolution reactions (HER) at the cathode. This prompted us to search for transition metal (TM) oxides capable of promoting efficient OER at the interfaces with a proton conducting ceramic electrolyte. Nevertheless, in many cases, well-established oxygen reduction

[a] Graduate School of Chemical Sciences and Engineering, Hokkaido University, N13W8, Kita-ku, Sapporo, 060-8628, Japan.
[b] Faculty of Advanced Science and Technology, Kumamoto University, 2-39-1 Kurokami, Chuo-ku, Kumamoto, 860-8555 Japan.
[c] Japan Synchrotron Radiation Research Institute (JASRI), 1-1-1, Kouto, Sayo-cho, Sayo-gun, Hyogo 679-5198 Japan.
[d] Institute of Multidsciplinary Research for Advanced Materials Research (IMRAM), Tohoku University, 2-1-1 Katahira, Sendai 980-8577, Japan.
[e] Faculty of Engineering, Hokkaido University, N13W8, Kita-ku, Sapporo, 060-8628, Japan.
† Corresponding author Email: y-aoki@eng.hokudai.ac.jp
Footnotes relating to the title and/or authors should appear here.
Electronic Supplementary Information (ESI) available: [details of any supplementary information available should be included here]. See DOI: 10.1039/x0xx00000x

reaction (ORR) cathodes of solid oxide fuel cells, i.e., perovskite-type cobaltites or manganites have been also applied as the OER anodes of SOECs; however, the anodic overpotentials of H^+-SOECs are still large in comparison with those of the cathodes of SOFCs. Hence, it is highly imperative to explore alternative anode candidates for developing highly efficient anode electrocatlysts for efficient H^+-SOECs.

High-valence TM cations incorporated into metal oxides are known to show high reactivity towards OER and ORR in neutral or alkaline solutions owing to their unique electronic structures.[11-17] The energy levels between the occupied metal d orbital and the O 2p orbital tend to get closer with increasing metal valence states, causing strong hybridization, and thus ligand-to-metal charge transfer states, such as $d^{n+1}\underline{L}^1$ and $d^{n+2}\underline{L}^2$, are intermixed with the typical ionic configuration $d^n\underline{L}^0$ in high-valence-state metal oxides.[18] Here, $\underline{L}$ represents the ligand hole (oxygen hole) and the superscript number indicates the electron or hole numbers on the metal d and oxygen 2p orbitals, respectively. In fact, the SOFC cathodes including high valence state Co^{3+} or Ni^{3+} cations involve intermixing of ligand hole states even at elevated temperatures, and such states are recognized to play a crucial role in the performance of the ORR cathode.[19,20] Hence, it is very important to explore OER anode materials based on high-valence-state TM oxides for highly efficient H^+-SOECs. Unfortunately, many such TM oxides are metastable phases under ambient atmosphere, as highlighted by their high redox potentials, which cause difficulty in using them directly in H^+-SOECs without reductive decomposition at elevated temperatures. $Ba_3(MnO_4)_2$ is a high-valence-state Mn(V) oxide that is known to be thermodynamically stable up to 1000°C in air, regardless of its unusual highly oxidized state,[21] and therefore, we adopted this oxide as a H^+-SOEC anode. Herein, we demonstrate that H^+-SOEC using a $Ba_3(MnO_4)_2$ base anode could achieve smaller anode polarization resistance than a cell with the well-known $Sm_{0.5}Sr_{0.5}CoO_3$ anode at ~700°C. $Ba_3(MnO_4)_2$ facilitates the chemisorption of water molecules onto the surface, because the abundant empty 3d states of high-valence Mn^{5+} cations allow its interaction with the electron-donating water, and thus provide a large reaction area that is spread over the entire grain surface instead of being limited within the gas-electrode-electrolyte triple phase boundary.

Experimental

Preparation and characterization

Barium manganate(V), $Ba_3(MnO_4)_2$, was prepared by a conventional solid-state reaction. The powders of $BaCO_3$ and $MnCO_3$ were mixed in an appropriate molar ratio and ground in a mortar for 1 h. The mixtures were then pelletized into a disc with a cold isostatic press (CIP) and calcined at 800°C for 6 h in ambient atmosphere. After pulverizing in the mortar, the powders were pelletized again by CIP and finally annealed at 950°C for 48 h in dry air (Ar/O_2 = 4/1). The resulting discs (9.3 mm ϕ, 1 mm d) were surface-scrubbed with alumina paste. The phase purity was confirmed by X-ray diffraction (RIGAKU Ultima-IV) with Cu *Kα* radiation, and chemical composition was examined by inductively-coupled-plasma optical emission analysis (ICP: Perkin-Elmer ICP-OES222) with the sample dissolved in 0.1 M H_2SO_4 solution. Lattice constants *a* and *c* were calculated by using following Eq. (1).

$$1/d_{hkl}^2 = (h^2+k^2+hk)/3a^2 + l^2/4c^2 \quad (1)$$

Here d_{hkl} is d-spacing of each Miller plane. The values of d_{hkl} were determined by XRD patterns calibrated with internal Si standard.

BET surface area was determined by acquiring nitrogen adsorption isotherms at 77 K (Microtrackbel BELSORP Mini-II). The electrical conductivity was measured with sintered $Ba_3(MnO_4)_2$ pellets by 4-probe DC measurements. The cylindrical pellets (5 mm ϕ × 15 mm L) were prepared by the same sintering process as mentioned above, and four Pt wires (0.05 mm ϕ) were wound on the rim of the pellets.

EXAFS

Operando XAFS for Mn K-edge was obtained on the BL01B1 station of SPring-8, Japan Synchrotron Radiation Research Institute (JASRI). The sample placed in the temperature-controllable cell was heated and/or cooled between room temperature and 700 °C at a heating rate of 10 °C min^{-1} in air (flow rate: 50 cm^3 min^{-1}). A Si(111) double-crystal monochromator was used. The incident and transmitted X-rays were monitored in ionization chambers filled with N_2 and 85% N_2 + 15% Ar. Quick EXAFS in the continuous scanning mode was recorded from 5674 to 7506 eV (5 min $scan^{-1}$). $BaMnO_4$ (Aldrich) and MnO_2 (Kanto) were used as reference samples. The specimens were mixed with boron nitride powder to achieve appropriate absorbance at the edge energy. The XAFS data were processed using the IFEFFIT software package (Athena and Artemis).

Steam electrolysis

Densely sintered pellets of $BaZr_{0.4}Ce_{0.4}Y_{0.2}O_{3-\delta}$ (BZCY442) were fabricated by a solid-state reactive sintering method assisted by zinc nitrate sintering additives. The precursor powder of BZCY442 was prepared by mixing stoichiometric amounts of the starting materials: $BaCO_3$ (High Purity Chemicals; 99.95%), CeO_2 (High Purity Chemicals; 99.99%), ZrO_2 (High Purity Chemicals; 98%), and Y_2O_3 (High Purity Chemicals; 99.99%) along with $Zn(NO_3)_2$ $6H_2O$ additive (Wako Chemicals; 99.9%) as a sintering aid. The amount of the added additive was adjusted for a Zn/Ba molar ratio of 0.02. The powders were dispersed in isopropanol, ball-milled for 24 h, and vacuum-dried. The obtained precursor powders were uniaxially pressed into green pellets at 20 MPa and subsequently pressed under a hydrostatic pressure of 100 MPa in an isostatic press. The pellets were sintered at 1400 °C for several hours in air, to obtain sintered discs with a typical diameter of ca. 9–9.2 mm and a thickness of 1.8–2.0 mm. Both sides of the sintered discs were polished with 1000 SiC abrasive sandpaper. The phase purity and crystallinity were verified by X-ray diffraction measurements with a RIGAKU diffractometer (RIGAKU Rint2000). Scanning electron microscopy (SEM) was

carried out on JEOL JSM-7100F microscope. The chemical compositions of the BCY thin films were examined by energy dispersive X-ray analysis (EDX) on JEOL JXA-8530F. The relative density of the sintered discs was measured using a pycnometer. The current-voltage (*I-V*) relationship and Faradaic efficiencies were evaluated in a two-electrode cell: 5% H_2/Ar, Pt | BZCY442 | oxide anode, 20% H_2O/air. The oxide anode and Pt cathode were screen-printed on the top and bottom surfaces of the BZCY sintered discs (1.5 mm thickness), respectively, using commercial or prepared pastes of cathode and anode catalysts, and these were subsequently co-fired at 800 °C. Pt was purchased from Tanaka Co. Here, three oxide materials were examined as an anode catalyst for steam electrolysis: $Sm_{0.5}Sr_{0.5}CoO_{3-\delta}$ (SSC), $Sb_{0.05}Sn_{0.95}O_{2-\delta}$ (ATO), and $Ba_3(MnO_4)_2$-ATO mixtures. SSC pastes were purchased from NexTech Materials Co., Ltd. ATO pastes were prepared by dispersing ATO powders (Mistubishi Materials Co.) in α-terpineol (Aldrich) with 5 wt% polymer dispersant (SolSphere 05). Pastes of $Ba_3(MnO_4)_2$-ATO were prepared by dispersing a $Ba_3(MnO_4)_2$/ATO mixture (6/4 weight ratio) in α-terpineol with 5 wt% polymer dispersant. The *I-V* characteristics were measured using a Solartron 1260/1287 system. The electrochemical impedance spectra of the SOEC were acquired using a Solartron 1260/1287 system in the frequency range of 10^6 to 0.1 Hz with an AC amplitude of 30 mV. To determine the Faradaic efficiency of the electrolysis reaction, electrolysis was carried out under galvanostatic conditions and the hydrogen concentrations in the anode out-gases were monitored by gas chromatography (Micro GC; Variant 2000).

Typically, humidified hydrogen gas (H_2O/H_2/Ar = 3/5/92) was fed to the Pt cathode side at a flow rate of 50 cm^3 min^{-1}, and a 20%-H_2O/air mixed gas (H_2O/O_2/Ar = 20/16/64) was fed to the anode side at a rate of 50 cm^3 min^{-1}. The 20%-H_2O/air mixed gas was prepared by passing air through a water bath maintained at ~60 °C and then supplied to the anode chamber through stainless-steel tubes heated to 150 °C with a ribbon heater to prevent condensation. Hence, the basic configuration of the SOEC is as follows: humidified air (H_2O/O_2/Ar = 20/16/64), SSC | BZCY | Pt, wet hydrogen (H_2O/O_2/Ar = 3/5/92).

Results

Electrical conductivity of $Ba_3(MnO_4)_2$

$Ba_3(MnO_4)_2$ has the $Ba_3(VO_4)_2$-type structure (hexagonal, $R\bar{3}m$), in which Ba cations have ten- or twelve-fold coordinated environments and Mn cations are in a slightly-distorted tetrahedral environment, existing as MnO_4^{3-}. The XRD pattern (Figure 1a) and the resultant lattice constants (a = 0.571 nm and c = 2.14 nm) are in agreement with those reported previously,[21] confirming that a single phase $Ba_3(MnO_4)_2$ was formed.

Figure 1b shows the normalized X-ray adsorption near edge structure (XANES) spectrum for Mn *K*-edge of $Ba_3(MnO_4)_2$ together with those of two references ($BaMn^{VI}O_4$ and $BaMn^{IV}O_3$), confirming that $Ba_3(MnO_4)_2$ has a well-adopted pentavalent manganese. $BaMn^{IV}O_3$. $Ba_3(Mn^{V}O_4)_2$ and $BaMn^{VI}O_4$ exhibit main adsorption peaks at 6556.1, 6557.7, and 6557.3 eV, respectively, attributed to the purely dipole-allowed 1s → 4p transition. Before the main edge peak, $Ba_3(Mn^{V}O_4)_2$ gives rise to a sharp pre-edge singlet at 6539.4 eV, due to the quadrupolar 1s → 3d transition arising from the hybridization of the 3d levels of Mn in the presence of the surrounding oxygen ligands.[22,23] This strong pre-edge feature is characteristics of tetrahedrally coordinated Mn atoms,[24] and thus, the tetrahedrally coordinated $BaMnO_4$ shows a strong peak at 6540.2 eV. The absorption edges defined as the middle point of the edge peaks are determined to be 6552.7, 6554.1 and 6554.8 eV for $BaMn^{IV}O_3$, $Ba_3(Mn^{V}O_4)_2$, and $BaMn^{VI}O_4$, respectively. Thus, the edge peak for $Ba_3(MnO_4)_2$ appears between those of the other two. This is in agreement with the general trends of manganese oxides, for which the absorption edge is linearly correlated with the nominal oxidation state.[24]

$Ba_3(MnO_4)_2$ exhibits poor semiconductor behavior: its electrical conductivity (σ) at room temperature is very small, at 4.1×10^{-6} S cm^{-1} (300°C) and does not increase above 3.7×10^{-3} S cm^{-1} even at 700°C (Figure 2a). σ shows an Arrhenius-type linear dependence on temperature (T) in the range below 520°C; however the plots clearly deviate upward for T higher than 550°C and the plots become again Arrhenius-type for T above 650°C, which implies the existence of second or higher order electronic transition in the temperature range of 550 to 650°C. The slopes clarify that the activation energy (E_a) of σ changes in the regions below 500°C and above 670°C, with the values being 72 and 48 kJ mol^{-1}, respectively. To verify the contribution of ionic conductivity, electromotive force (*EMF*) measurements were conducted by constructing oxygen concentration cells (2%-O_2/Ar, Pt | $Ba_3(MnO_4)_2$ | Pt, 100%- O_2) and water concentration cells (0.5%-H_2O/air, Pt | $Ba_3(MnO_4)_2$ | Pt, 20%-H_2O/air) at 600 and 700°C. Both cells do not yield significant *EMF* at either temperature, proving that the electron charge carriers (or hole) are dominant and the proton and oxide ion transfer numbers are negligible over all temperature ranges, and thus, the jump in σ at ~650°C can be attributed to the change in the electron conduction mechanism.

High-temperature XRD reveals that structural deformation takes place together with the conductivity jump at ~650°C. $Ba_3(MnO_4)_2$ retains the original crystalline phase even at 800°C (Supplementary Figure 1S). The (300) XRD peak essentially shifts to the lower 2θ side with increasing temperature (Figure 2b), and thus the lattice constants increase continuously with heating (Figure 2c), which is attributed to the thermal expansion of unit cells along a-axis. On the other hand, (205) peak shifts to lower 2θ side with temperature in the region of T < 690°C but is fixed in the range of T > 700°C (Figure 2b), resulting in the shrink of unit cell along c-axis with temperature in T > 700°C (Figure 2c). Similarly the unit cell volume (V) increases with temperature in T < 690°C but tends to decrease in T > 700°C (Figure 2c), confirming that conductivity jump takes place with thermal shrinkage of V.

XAFS analysis

In order to elucidate the rearrangement of the local structure around Mn atoms at elevated temperatures, *operando* Mn *K*-edge XAFS was conducted for $Ba_3(MnO_4)_2$ under ambient

atmosphere. Figure 3a shows the normalized XANES spectrum of $Ba_3(MnO_4)_2$. The spectrum remained unchanged with heating at temperatures below 600°C, while the intensity of the pre-edge and main adsorption peaks abruptly decreased with heating between 600 and 700°C, implying the modification of the local coordination environment around Mn atoms due to structural deformation at T > 600 °C.

Fourier-transform EXAFS analysis was performed to investigate the deformation of the $Mn^{v}O_4^{3-}$ tetrahedron with heating (Table 1 and Figure 3b). Since these data are shown without phase-shift corrections, the observed peaks might yield shorter atomic distance values than the true atomic distances. Nevertheless, for $Ba_3(MnO_4)_2$, the first coordination shell corresponding to an intense peak at ~1.45 Å can be attributed to the bonding of Mn with four corner O atoms for the $Mn^{v}O_4^{3-}$ tetrahedral oxoanions. In $Ba_3(MnO_4)_2$, MnO_4 tetrahedra take C_{3v} symmetry with one shorter Mn-O2 bond (1.671 Å) and three longer Mn-O1 bonds (1.705 Å).[21] The curve-fitting analysis of the first coordination shell of $Ba_3(MnO_4)_2$ at 25°C leads to a tetrahedral coordination environment with three oxygen atoms at a distance of 1.70 Å and one oxygen at a distance of 1.66 Å (Table 1), which are consistent with the aforementioned features of $Mn^{v}O_4^{3-}$ oxoanions.[21] The profiles at 400 and 600°C could be fitted very well by a similar C_{3v} symmetric coordination model, confirming that the local coordination environment around Mn atoms remains unchanged at T < 600°C (Table 1 and Figure 3b). In contrast, the EAXFS at 700 °C does not account for the C_{3v} symmetric tetrahedral coordination environment. The peak position of the first coordination shell clearly shifts to the shorter side with heating between 600 and 700°C (Figure 3b), indicating a decrease in the average Mn−O bond length of the $Mn^{v}O_4^{3-}$ tetrahedron. The best fitting for the first Mn−O shell is obtained by T_d symmetric tetrahedral coordination environment with four oxygen atoms at an equidistance of 1.69 Å, and this value lies between those of the shorter Mn-O2 bond and longer Mn-O1 bond lengths of the room-temperature phase (Table 1 and Figure 3b). Combined EXAFS and XRD studies provide a clear physical model for the structural deformation with the abrupt change in conductivity at ~650 °C (see Figure 4). In $Ba_3(MnO_4)_2$, an O^{2-} anion tightly-bonded to a Mn^{5+} cation (O2) is also coordinated by a Ba^{2+} cation, and thus, the Mn, O, and Ba atoms are aligned along the c-axis. In this part, the O atoms bind more tightly to Mn than to Ba neighbors at room temperature, owing to the shorter Mn-O2 bond, which leads to the maintenance of distance between Ba and O neighbors in the phase before conductivity jump. However, the Ba cations tend to attract the O neighbors more tightly in the phase at T > 650°C than in the phase at T < 600°C, and therefore, the lattice constant c contracts at ~650 °C.

Since $Ba_3(MnO_4)_2$ is a spin-dimer antiferromagnet with a high-spin configuration of S = 1,[25] the conductivity gap is close to the sum of band gap (E_g) and exchange energy for antiferromagnetic ordering (J). The antiferromagnetic/ paramagnetic transition above Neel temperature is typical of second order phase transition,[26] which is in agreement with the feature of conductivity jump of $Ba_3(MnO_4)_2$. The conductivity gap of paramagnetic phase tends to be smaller than that of antiferromagnetic phase due to the decline of the exchange term, and thus, the conductivity jump is attributable to antiferromagnetic/ferromagnetic transition. The shape change of MnO_4 units must be correlated to the phase transition.

Steam electrolyzer cells

The steam electrolysis was conducted with a cell of oxide-anode | BZCY442 (1.5 mm) | Pt-cathode fed with humidified air (20% H_2O) at the anode side and humidified 1%-H_2/Ar gas (3% H_2O) at the cathode side. Supplementary Figure S2 shows a surface SEM images of the SSC, $Ba_3(MnO_4)_2$, and $Ba_3(MnO_4)_2$–ATO mixture anode layers formed on BZCY sintered discs, confirming that all are porous and comprise agglomerates of sub-micrometer- or micrometer-sized particles. The sizes of SSC and ATO particles are ~200 nm and less than 50 nm, respectively, and thus have relatively large BET surface areas of 39 and 115 $m^2\ g^{-1}$, respectively. In contrast, $Ba_3(MnO_4)_2$ powders are made of coarse grains with 0.5–3 μm diameters and thus have a relatively small BET surface area of 9.5 $m^2\ g^{-1}$, which indicates that $Ba_3(MnO_4)_2$-ATO anodes are made of agglomerates of large $Ba_3(MnO_4)_2$ grains deposited with small ATO particles.

The I-V characteristics of the steam electrolyzers with SSC and $Ba_3(MnO_4)_2$-ATO anodes at 700 and 600°C are shown in Figure 5a. Both cells have OCVs of ~0.95 and 1.02 V at 700 and 600 °C, respectively, which are in agreement with the values reported for the $BaZr_xCe_{0.8-x}Y_{0.2}O_{3-\delta}$ cells fed with diluted hydrogen and steam.[27-31] In contrast, ATO showed deteriorated performance, with an OCV of less than 0.6 V and much smaller current than those of the other two at any temperature (Figure 5a). These results indicate that ATO is not electrocatalytically active, and it therefore acts only as an electroconductive filler. The electrolysis current of $Ba_3(MnO_4)_2$-ATO is remarkably larger than that of SSC at 700 °C, with the currents at 2.0 V bias for $Ba_3(MnO_4)_2$-ATO and SSC cells being 125 and 80 mA cm^{-2}, respectively. However, the current of the former falls to a similar level as that of the latter with a decrease in the temperature to 600 °C, with the currents at 2.0 V bias for SSC and $Ba_3(MnO_4)_2$-ATO cells equaling 40 mA cm^{-2}.

The Faradaic efficiency of $Ba_3(MnO_4)_2$-ATO was examined by monitoring the amount of hydrogen gas evolved on the cathode side under galvanostatic conditions, confirming that the $Ba_3(MnO_4)_2$ cell facilitates steam electrolysis as highly efficiently as the SSC cell.[32]At 700 °C, the efficiency is more than 80% in the current range of less than 50 mA cm^{-2}, whereas it drops to 70% under high current conditions (Figure 5b). Such a characteristic has been attributed to the increase in the partial hole conductivity of the $BaZr_xCe_{0.8-x}Y_{0.2}O_{3-\delta}$ electrolyte at elevated temperatures.[33–35] Hence, the cell yields a higher Faradaic efficiency with decreasing temperature, due to a decrease in the hole transfer numbers, thus achieving ~75% efficiency at 600 °C (Figure 5b). The SSC cell exhibits similar efficiency as the $Ba_3(MnO_4)_2$ cell.[32]

To deconvolute the anodic polarization resistances, the impedance responses were recorded at 700 °C under various DC conditions (Figure 6). In general, in the impedance spectra of solid electrochemical cells, the high-frequency x-intercept

represents Ohmic loss, i.e. the electrolyte resistances and the following arcs are associated with the interfacial polarization. SSC cells yield two distinct arcs at 700 °C: a large S_h arc in the high-frequency region at approximately 10^5–10^2 Hz, and a small S_l arc in the low-frequency region at approximately 10^2–10^{-1} Hz. These spectral features of the SSC cells at 700 °C have been replicated well by employing the equivalent circuit shown in the inset of Figure 7a,[32] wherein R_b corresponds to the electrolyte resistance and the parallelly connected elements (R_hQ_h) and (R_lQ_l) represent S_h and S_l impedance arcs, respectively. Here, R_i is a resistance element and Q_i is a constant phase element representing the time-dependent capacitance,[36] and the parallelly connected R_i and Q_i are related to the capacitance C_i according to Eq. (2).[36]

$$C_i = (R_i \cdot Q_i)^{1/ni} R_i^{-1} \quad (2)$$

The spectra obtained at various potentials can be fitted with the equivalent circuit $R_b(Q_hR_h)(Q_lR_l)$, and R_i, Q_i, and n_i can be determined with errors within a few tens of percentage points. $Ba_3(MnO_4)_2$-ATO cells also provide two impedance arcs at 700°C, which appear in the same frequency regions as S_h (10^4–10^2 Hz) and S_l (10^2–10^{-1} Hz). The diameter of both arcs systematically decreases with increasing DC current (Figure 6a), revealing that these are related to the anode reaction kinetics and not the diffusion-limited concentration overpotentials. The diameters of the mixed S_h and S_l arcs of the $Ba_3(MnO_4)_2$-ATO anode are nearly half those of SSC anode, confirming that polarization resistances of the former are much smaller than those of the latter. The spectra of $Ba_3(MnO_4)_2$-ATO can be also fitted very well with the same equivalent circuit as that used for the SSC cell (Figure 7a). The R_b is approximately 7–8 Ω cm^2 at all potentials, which is much larger than the polarization resistances R_h and R_l, indicating that the electrolyte resistance dominates over all voltage losses, even at 700 °C, owing to the significant thickness (1.2 mm) of the bulk electrolytes. The resultant R_h and R_l for SSC and $Ba_3(MnO_4)_2$-ATO cells are plotted as a function of cell voltage in Figure 7b. Whereas both have similar R_l values, R_h is significantly reduced upon using $Ba_3(MnO_4)_2$-ATO anode.

The cells exhibited elongated polarization arcs at 600 °C (Figure 6b) because additional polarization arcs appeared in the mid-frequency region at ~10^2 Hz with decreasing temperature. Unfortunately, it is difficult to conduct equivalent circuit fitting to such an elongated spectrum on the basis of a simple parallelly connected (Q_iR_i) component. The diameters of the mixed impedance arcs of $Ba_3(MnO_4)_2$-ATO and SSC are similar, implying that the polarization resistances of the former are similar to those of the latter at 600°C. This is consistent with the results of *I-V* characteristics (Figure 5a), proving that the electrocatalytic activity of $Ba_3(MnO_4)_2$ is enhanced by the conductivity jump. Hereafter, the properties at 700 °C are mainly accounted for.

Discussion

We demonstrated that $Ba_3(MnO_4)_2$ has a pronounced electrocatalytic performance for anode reactions of H^+-SOEC at *T* above 600 °C with a conductivity jump. Polarization resistances of the $Ba_3(MnO_4)_2$-base anode are sufficiently lower than those of the well-established SSC anode aided by a conductive filler at 700 °C, although the values of the former fall to the same level as those of the latter at 600 °C, before electronic conduction jump.

Recently, two kinds of reaction scheme have been proposed for the OER of H-SOEC;[32] one is triggered by water adsorption on the anode surface (Model-A; Figure 8a),[30] while the other is triggered by water adsorption at the gas-electrode-electrolyte triple phase boundary (TPB) (Model-B; Figure 8b).[37] In Model-A, the OER process is completed via dissociative adsorption of water on the electrode surface (step-1a, 2a and 3a), multiple charge transfers (step-4a and 5a), and associative adsorption of oxygen on the electrode surface (step-6a and 7a), together with interfacial proton transfer across the TPB (step-8a and 9a), as shown in Figure 8a and Table 2.[32] Here "ad," "TPB," and "elec" indicate species in the electrode surface, the TPB, and the BZCY electrolyte, respectively. In Model-B, the OER process comprises dissociative adsorption of water at the TPB (step-1b, 2b and 3b), multiple charge transfers with the shift of oxygen species (step-5b, 6b and 7b), and associative adsorption of oxygen on the electrode surface (step-8b), together with interfacial proton transfer (step-4b), as shown in Figure 8b and Table 2.[32]

According to simple kinetic treatment, the rate equations for the elementary steps were converted to a function of p_{O2}^m and p_{H2O}^n with reaction orders of *m* and *n*, as listed in Table 2.[32] If step-i with reaction orders of m_i and n_i is the rate-controlling anode reaction of SOEC, ideally, the corresponding polarization resistances (R_i) should be proportional to p_{O2}^{-mi} and p_{H2O}^{-ni}. Based on this assumption, the impedance analysis with varying p_{O2} and p_{H2O} at anode sides have been carried out for the SSC cell to determine the reaction orders of R_h and R_l.[32] The anode reactions at the SSC/BZCY interfaces were found to proceed via the pathway of Model-B.[32] Moreover, the S_h of SSC cells could be assigned to the first electron transfer at TPB (step-5b) and S_l to the shift of the oxygen chemisorbed from TPB to the anode surface (step-6b) because the measurements provided $R_h \propto p_{O2}^0$ and p_{H2O}^0 and $R_l \propto p_{O2}^{-1/4}$ and p_{H2O}^0, which are in agreement with the ideal reaction orders of each step in Model-B (Table 2).[32]

To gain insight into the reaction scheme and rate-limiting steps for the $Ba_3(MnO_4)_2$ base anode, impedance responses were acquired in terms of p_{O2} and p_{H2O} in anode gases (Figure 8c-f). As for the p_{O2} dependence, S_l arcs are remarkably enlarged with decreasing p_{O2}, with R_l being proportional to $p_{O2}^{-0.32}$ (Figure 8c and d) in the p_{O2} range of 0.02 to 1.0 p_0 (p_0 = 101.3 kPa) at a fixed temperature. S_h arcs are weakly dependent on p_{O2}, leading to $R_h \propto p_{O2}^{-0.13}$. For p_{H2O} dependence, however, $Ba_3(MnO_4)_2$ yields a negative value of *n* for both S_h and S_l arcs (Figure 8e and f). R_h and R_l significantly increase with p_{H2O} in the range of 0.01 to 0.5 p_0, indicating the deterioration of the electrocatalytic performance of $Ba_3(MnO_4)_2$ due to moisture. XRD measurements confirm that $Ba_3(MnO_4)_2$ and ATO remain unchanged even after steam electrolysis at 2.0 V for 1 h (Supplementary Figure S3). Furthermore, the impedance arcs of $Ba_3(MnO_4)_2$-ATO can recover their original values with the return of p_{H2O} to 0.1p_0 after exposure to 50%-H_2O/air for 3 h

(Figure 8b), confirming that $Ba_3(MnO_4)_2$ does not decompose at high p_{H2O} conditions. These features imply that $Ba_3(MnO_4)_2$ suffers H_2O-poisoning under relatively high p_{H2O}, probably owing to the strong interaction between H_2O and $Ba_3(MnO_4)_2$: the surface coverage by adsorbed H_2O increases and the number of reaction sites is decreased with increasing p_{H2O}.

Nevertheless, the p_{H2O} dependence provides a clear evidence for the occurrence of OER on $Ba_3(MnO_4)_2$ via a different reaction scheme than that of SSC, i.e., via Model-A. m of R_h is ~0.13, which is in agreement with the ideal values (1/8) of step-4a (1st electron (hole) transfer step) in Model-A, while it does not conform to any steps of Model-B (Table 2). Similarly, m of R_l results in 0.32, which is consistent with the value (3/8) of the second electron transfer step, i.e., step-5a, but is not close to the values of Model-B. These results prove that the anode reaction processes on the $Ba_3(MnO_4)_2$ base anode mainly occur according to Model-A, although those of the SSC cells are driven by Model-B. Moreover, the results of the reaction order analysis suggest that the electron charge transfers steps would limit the overall reaction rate of the $Ba_3(MnO_4)_2$ anode (Figure 8a), probably owing to its poor electrical conductivity. Since σ of $Ba_3(MnO_4)_2$ is several orders of magnitude lower than that of SSC (~500 S cm^{-2} at 700 °C)[38] even after the conductivity jump, large overpotentials may take place for driving electron migration in $Ba_3(MnO_4)_2$. In fact, $Ba_3(MnO_4)_2$ cannot achieve pronounced electrocatalytic performance before the conductivity jump at ~600 °C.

The aforementioned results unambiguously demonstrate that $Ba_3(MnO_4)_2$ is greatly advantageous for use in H^+-SOEC in relation to the extended reaction areas. Since $Ba_3(MnO_4)_2$ allows water adsorption, the effective reaction sites are extended over the entire electrode surface without being confined near the TPB. However, the reaction sites of the SSC anode are limited, since the water adsorption is triggered only at the TPB, owing to the relatively high hydration enthalpy.[39] Hence, $Ba_3(MnO_4)_2$ anode exhibits lower anode polarization resistances than SSC although the former has a smaller TPB area than the later owing to the relatively large grain size. The interaction of water with metal oxides is largely studied both experimentally and theoretically, and it has been accepted that water molecule acts as an electron-donor on semiconductor oxides.[40-42] An n-type semiconductor $SrSnO_3$ causes resistance changes by responding to water adsorption/desorption, since the chemisorbed water donates electrons to the metal oxide and thus its resistance decreases when exposed to humidity.[43] Based on this criterion, the chemisorption of water is thermodynamically favorable for $Ba_3(MnO_4)_2$, because the high-valence-state Mn has many unoccupied 3d states to accept the additional electrons. In conclusion, $Ba_3(MnO_4)_2$ is a promising anode electrocatalyst for H^+-SOEC, and this finding offers an opportunity to explore other active anode materials based on high-valence-state transition metal oxides.

Conclusions

Herein, high-valence-state Mn(V) oxide $Ba_3(MnO_4)_2$ was demonstrated to be a promising anode electrocatalyst of H^+-SOECs. $Ba_3(MnO_4)_2$ exhibited poor semiconductor behavior while the conductivity increased by one order of magnitude at ~600 °C, owing to the antiferromagnetic/paramagnetic phase transition, accompanied by a shape change of tetrahedral MnO_4^{3-} anions. Anode reactions with SSC anode, which is a well-known electrode material for H^+-SOEC, is driven by the adsorption of water at the TPB and subsequent surface diffusion of oxygen species, since the hydration of cobaltite is not thermodynamically favored. However, $Ba_3(MnO_4)_2$ anode is found to facilitate OER directly with the surface-adsorbed water, because many unoccupied 3d states of the high-valence-state Mn^{5+} cations are favorable to accept additional electrons and thus adsorption of water electron donors is facilitated. Thus, $Ba_3(MnO_4)_2$ base anode exhibits a lower polarization resistance than that of SSC, because of the extension of the reaction area over the entire surface. The current results offer an opportunity to explore more active anode materials based on high-valence-state transition metal oxides.

Conflicts of interest

There are no conflicts to declare.

Acknowledgements

This work was supported by the JST MIRAI “Realization of a low carbon society, global issue”, No. JPMJM17E7; JSPS KAKENHI: Grant-in-Aid for Scientific Research (B), No. 18H02066, JSPS KAKENHI: Grant-in-Aid for Young Scientists (B), No. 17K14114, and the "Nanotechnology Platform" program of the MEXT Japan.

Notes and references

‡ Footnotes relating to the main text should appear here. These might include comments relevant to but not central to the matter under discussion, limited experimental and spectral data, and crystallographic data.

§

§§

etc.

1 S. D. Ebbesen, S. H. Jensen, A. Hauch and M. B. Mogensen, *Chem. Rev.,* 2014, **114**, 10697.
2 M. Ni, M. K. H. Leung and D. Y. C. Leung, *Int. J. Hydrogen Energy,* 2008, **33**, 2337.
3 A. Hauch, S. D. Ebbesen, S. H. Jensen and M. Mogensen, *J. Mater. Chem.*, 2008, **18**, 2331.
4 X. Yang and J. T. S. Irvine, *J. Mater. Chem.,* 2008, **18**, 2349.
5 T. Matsui, R. Kishida, J. Y. Kim, H. Muroyama and K. Eguchi, *J. Electrochem. Soc.*, 2010, **157**, B776.
6 K. D. Kreuer, *Annu. Rev. Mater. Res.*, 2003, **33**, 333.
7 H. Iwahara, *Solid State Ionics,* 1996, **9**, 86.
8 H. Iwahara, H. Uchida, K. Ono and K. Ogaki, *J. Electrochem. Soc.*, 1988, **135**, 529.
9 L. Bi, S. Boulfrad and E. Traversa, *Chem. Soc. Rev.,* 2014, **43**, 8255.
10 K. Zeng and D. Zhang, *Prog. Energy. Combustion Sci.*, 2010, **36**, 307.
11 A. Grimaud, O. Diaz-Morales, B. Han, W. T. Hong, Y. Lee, L. Giordano, K. A. Stoerzinger, Marc T. M. Koper and Y. Shao-Horn, *Nature Chem.,* 2017, **9**, 457.

12 J. Suntivich, K. J. May, Hubert A. Gasteiger, John B. Goodenoug and Yang Shao-Horn, *Science,* 2011, **334**, 1383.
13 A. Grimaud, K. J. May, C. E. Carlton, Y. Lee, M. Risch, W. T. Hong, J. Zhou and Y. Shao-Horn, *Nature Commun.,* 2013, **4**, 2439.
14 F. Calle-Vallejo, Oscar A. Díaz-Morales, Manuel J. Kolb and Marc T. M. Koper, *ACS Catal.,* 2015, **5**, 869.
15 Xi Rong, J. Parolin and A. M. Kolpak, *ACS Catal.,* 2016, **16**, 1153.
16 S. Yagi, I. Yamada, H. Tsukasaki, A. Seno, M. Murakami, H. Fujii, H. Chen, N. Umezawa, H. Abe, N. Nishiyama and S. Mori, *Nature Commun.*, 2015, **6**, 8249.
17 I. Yamada, A. Takamatsu, K. Asai, T. Shirakawa, H. Ohzuku, A. Seno, T. Uchimura, H. Fujii, S. Kawaguchi, K. Wada, H. Ikeno and S. Yagi, *J. Phys. Chem. C*, 2018, **122**, 27885-27892.
18 Z. Lu, H. Wang, D. Kong, K. Yan, P. Hsu, G. Zheng, H. Yao, Z. Liang, X. Sun and Y. Cui, *Nature Commun.,* 2014, **5**, 4345.
19 D. N. Mueller, M. L. Machala, H. Bluhm and W. C. Chueh, *Nature Commun.*, 2015, **6**, 6097.
20 T. Nakamura, R. Oike, Y. Kimura, Y. Tamenori, T. Kawada and K. Amezawa, *ChemSusChem,* 2017, **10**, 2008.
21 M. T. Weller and S. J. Skinner, *Acta Cryst.,* 1999, **C55**, 154-156.
22 T. Yamamoto, *X-Ray Spectrom.,* 2008, **37**, 572.
23 C. F. Petersburg, Z. Li, N. A. Chernova, M. S. Whittingham and Faisal M. Alamgir, *J. Mater. Chem.*, 2012, **22**, 19993.
24 F. Farges, *Phys. Rev. B*, 2005, **71**, 155109.
25 M. Uchida, H. Tanaka, H. Mitamura, F. Ishikawa and T. Goto, *Phys. Rev. B*, 2002, **66**, 054429/1–6.
26 C. N. R. Rao, *Annu. Rev. Phys. Chem.*, 1989, **20**, 291-326.
27 L. Bi, S. P. Shafi and E. Traversa, *J. Mater. Chem. A*, 2015, **3**, 5815.
28 Y. Gan, J. Zhang, Y. Li, S. Li, K. Xie and J. T. S. Irvine, *J. Electrochem. Soc.*, 2012, **159**, F763.
29 P. A. Stuart, T. Unno, J. A. Kilner and S. J. Skinner, *Solid State Ionics*, 2008, **179**, 1120.
30 F. He, D. Song, R. Peng, G. Meng, and S. Yang, *J. Power Sources*, 2010, **195**, 3359.
31 S. Li, and K. Xie, *J. Electrochem. Soc.*, 2013, **160**, F224.
32 T. Kobayashi, K. Kuroda, S. Jeong, H. Kwon, C. Zhu, H. Habazaki and Y. Aoki, *J. Electrochem. Soc.*, 2018, **165**, F342.
33 H. Zhu, S. Ricote, C. Duan, R. P. O'Hayre, D. S. Tsvetkov and R. J. Kee, *J. Electrochem. Soc.*, 2018, **165**, F581.
34 M. Oishi, S. Akoshima, K. Yashiro, K. Sato, J. Mizusaki and T. Kawada, *Solid State Ionics*, 2008, **179**, 2240.
35 M. Dippon, S. M. Babiniec, H. Ding, S. Ricote, and N. P. Sullivan, *Solid State Ionics*, 2016, **286**, 117.
36 A. Bierberle-Hütter, M. Sogaard, and H. L. Tuller, *Solid State Ionics*, 2006, **172**, 1969.
37 F. He, T. Wu, R. Peng, and C. Xia, *J. Power Sources*, 2009, **194**, 263.
38 S. Yang, T. He and Q. He, *Journal of Alloys and Compounds*, 2008, **450**, 400.
39 R. Zohourian, R. Merkle, and J. Maier, *Solid State Ionics*, 2017, **299**, 64.
40 J. Park, J. Jeong, H. Chung, Y. Mo and H. Kim, *Appl. Phys. Lett.*, 2008, **92**, 072104.
41 M. Ni, M. K.H. Leung, D. Y.C. Leung and K. Sumathy, *Renewable Sustainable Energy Rev.*, 2007, **11**, 401.
42 A. Calzolari and A. Catellani, *J. Phys. Chem. C*, 2009, **113**, 2896.
43 Y. Shimizu, M. Shimabukuro, H. Arai and T. Seiyama, *J. Electrochem. Soc.*, 1989, **136**, 1206.

FIGURE CAPTIONS

Figure 1 (a) XRD patterns of $Ba_3(MnO_4)_2$. (b) Mn K-edge XANES of $Ba_3(MnO_4)_2$ and references of $BaMnO_4$ and $BaMnO_3$.

Figure 2 (a) Electrical conductivity of $Ba_3(MnO_4)_2$ in air. (b) High-temperature XRD of $Ba_3(MnO_4)_2$, showing shifts of (202) and (300) peaks with temperature. (c) Variation of lattice constants *a* and *c* and unit cell volumes *V*.

Figure 3 Mn K-edge EXAFS of $Ba_3(MnO_4)_2$ at various temperatures. (a) XANES region and (b) the corresponding Fourier-transformed radial distribution functions. The inset in (a) shows an expansion of the adsorption edge.

Figure 4 Structural deformation and decreasing conductivity gap by the antiferoganetic/paramagnetic transitions.

Figure 5 (a) *IV*-characteristics of SOEC with $Ba_3(MnO_4)_2$-ATO, ATO, and SSC anodes. Solid and dashed lines indicate the currents at 700 and 600 °C. (b) Hydrogen evolution rate of SOEC with $Ba_3(MnO_4)_2$-ATO (○) and SSC (△) anodes at 700 and 600 °C.

Figure 6 Impedance responses of SOEC with SSC or $Ba_3(MnO_4)_2$-ATO anodes at (a) 700°C and (b) 600°C under various biases. 20%-H_2O/air was fed to the anode and 3%-H_2O/5%-H_2/Ar was fed to the cathode. In (a), S_h and S_l indicate the impedance arcs in high and low frequency ranges, respectively. The details are provided in the text

Figure 7 (a) Equivalent circuit fitting to the impedance spectra of SOEC with or $Ba_3(MnO_4)_2$-ATO anodes at 700 °C under 0.2 V cell voltage. Circles represent the measured data and solid line represents the fit with the model depicted in the inset. (b) R_h (circles) and R_l (triangles) of the impedance spectra of SOEC with SSC or $Ba_3(MnO_4)_2$-ATO anode under various DC conditions at 700 °C, which were determined by equivalent circuit analysis of the spectra displayed in Figure 6 (a).

Figure 8 Schemes for the anode reactions of H^+-SOEC with the reaction sites existing (a) over the electrode surface and (b) at the gas-electrode-electrolyte triple phase boundary. Impedance responses of SOEC with $Ba_3(MnO_4)_2$-ATO anodes, obtained by changing (c) p_{O2} and (e) p_{H2O} in the anode side at 700 °C. Circles are the observed values and solid lines are the fits obtained by equivalent circuit analysis with the model depicted in Fig. 7(a). Resultant R_h and R_l determined by equivalent circuit analysis of (d) p_{O2} and (f) p_{H2O}-variable impedance spectra.

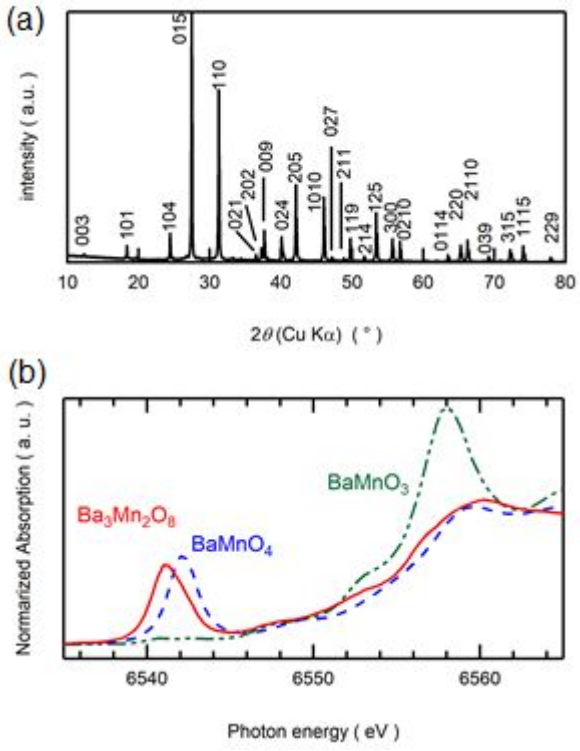

Figure 1 (a) XRD patterns of $Ba_3(MnO_4)_2$. (b) Mn K-edge XANES of $Ba_3(MnO_4)_2$ and references of $BaMnO_4$ and $BaMnO_3$.

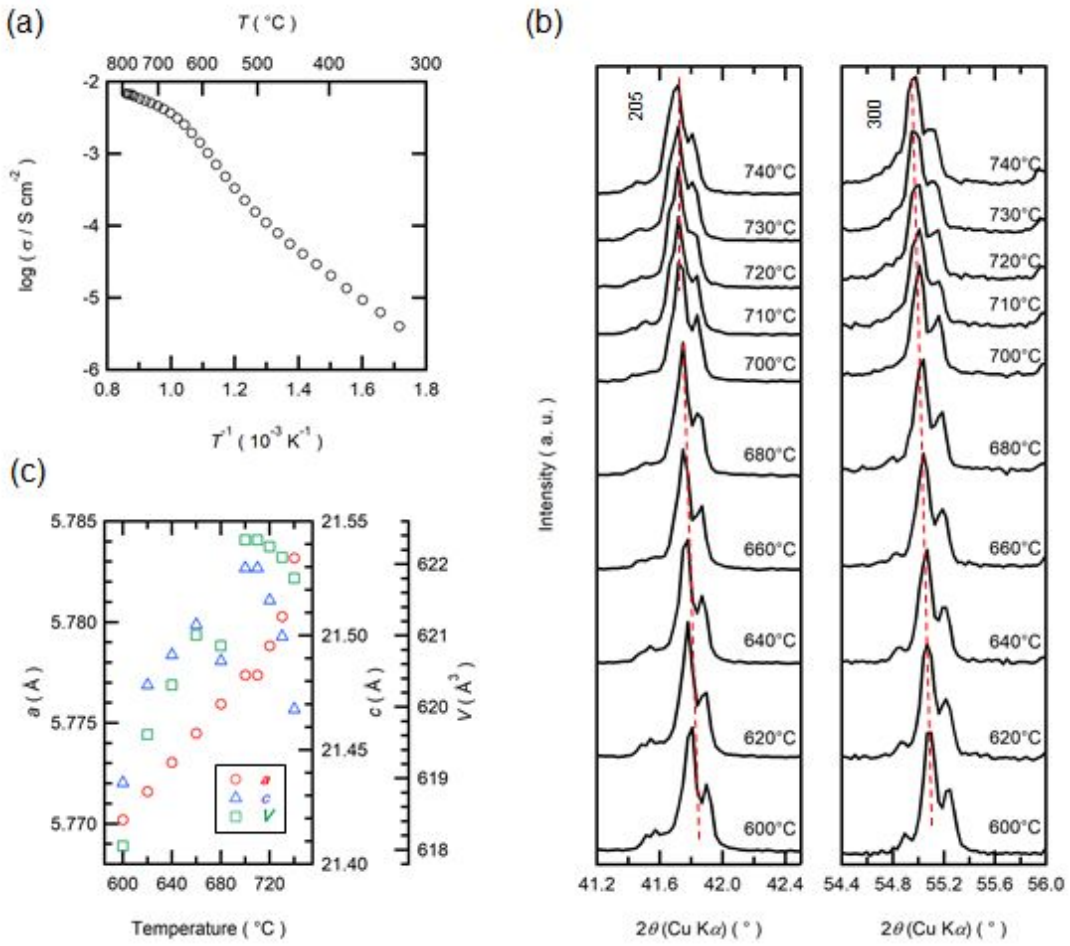

Figure 2 (a) Electrical conductivity of $Ba_3(MnO_4)_2$ in air. (b) High-temperature XRD of $Ba_3(MnO_4)_2$, showing shifts of (202) and (300) peaks with temperature. (c) Variation of lattice constants *a* and *c* and unit cell volumes *V*.

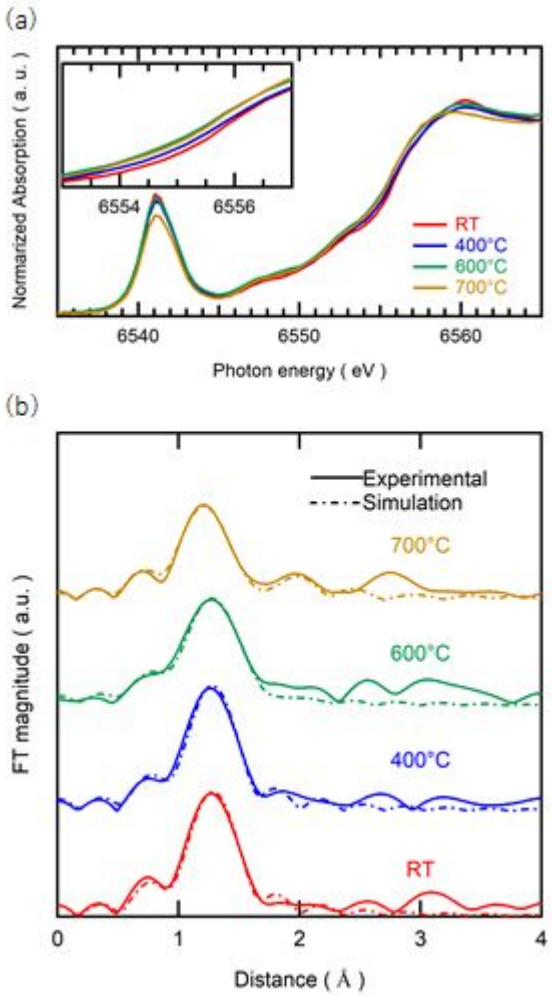

Figure 3 Mn K-edge EXAFS of $Ba_3(MnO_4)_2$ at various temperatures. (a) XANES region and (b) the corresponding Fourier-transformed radial distribution functions. The inset in (a) shows an expansion of the adsorption edge.

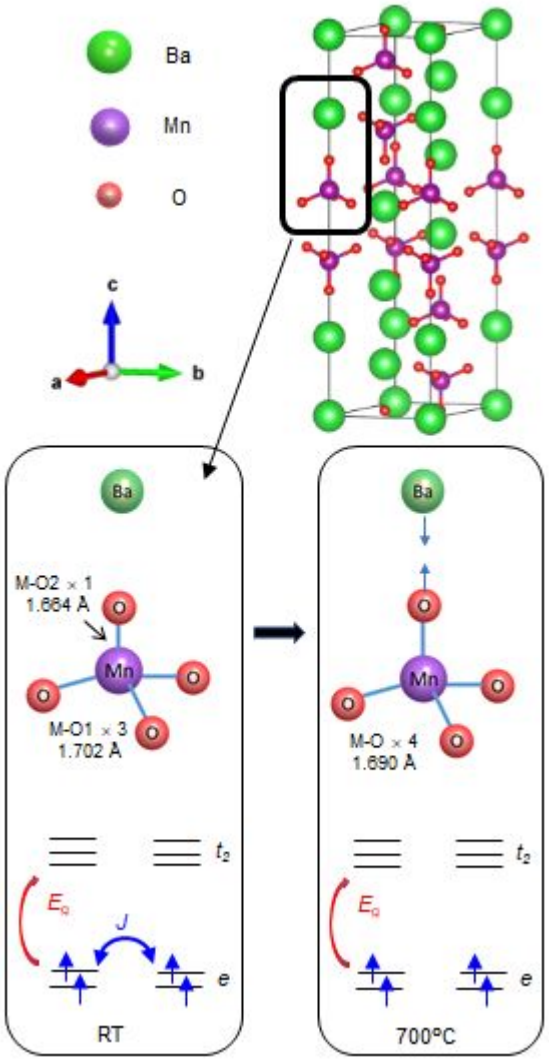

Figure 4 Structural deformation and decreasing conductivity gap by the antiferogaetic/paramagnetic transitions.

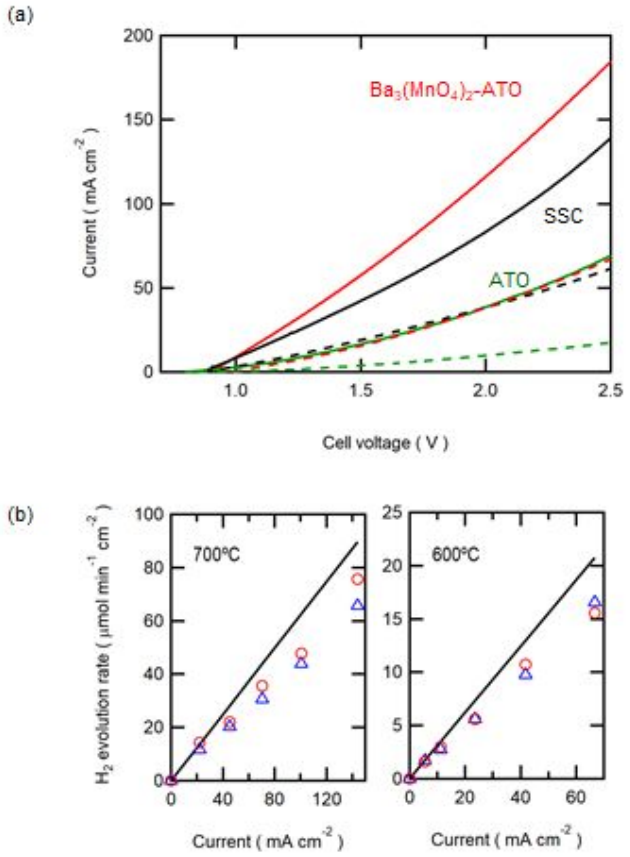

Figure 5 (a) *IV*-characteristics of SOEC with $Ba_3(MnO_4)_2$-ATO, ATO, and SSC anodes. Solid and dashed lines indicate the currents at 700 and 600 °C. (b) Hydrogen evolution rate of SOEC with $Ba_3(MnO_4)_2$-ATO (○) and SSC (△) anodes at 700 and 600 °C.

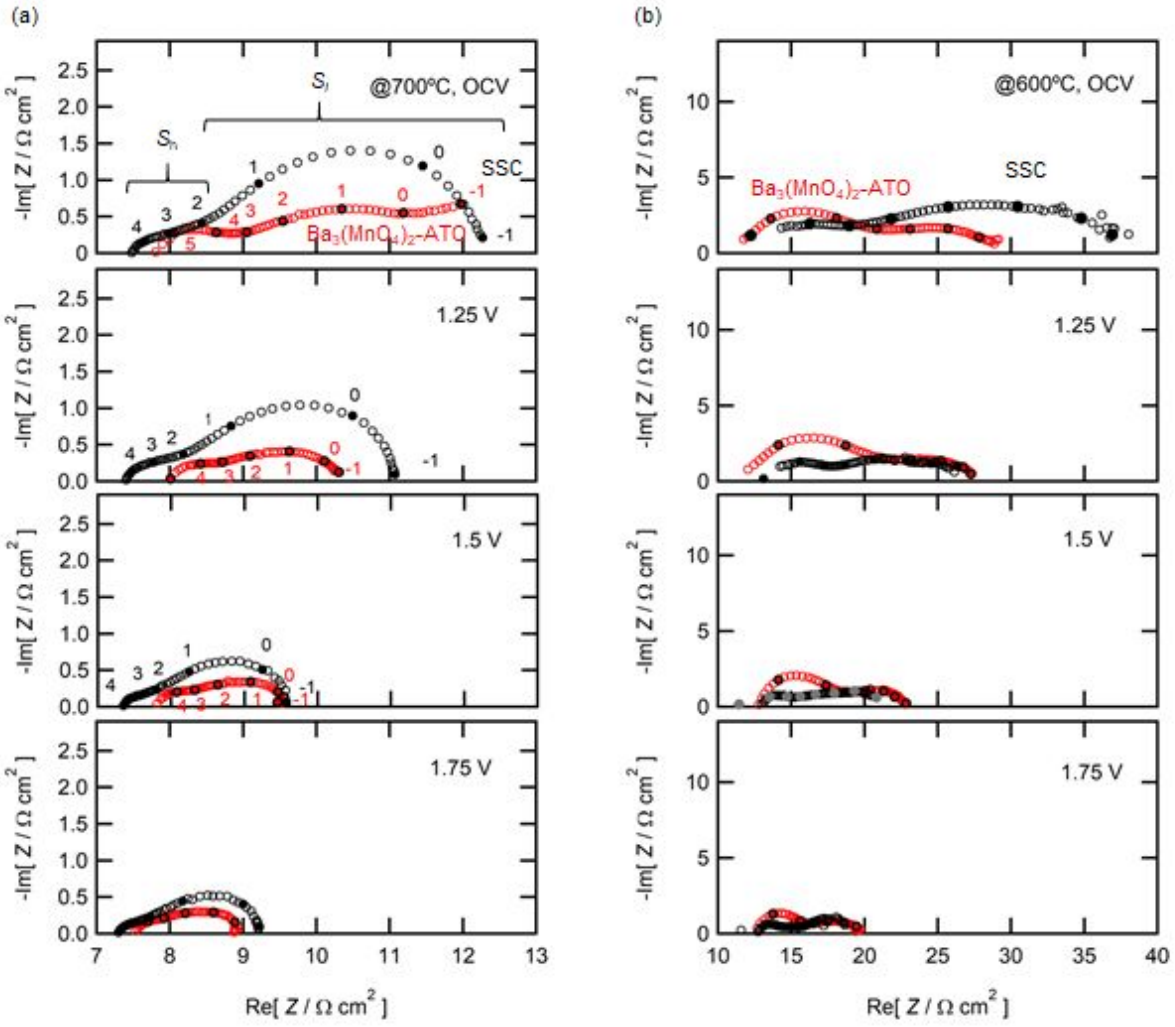

Figure 6 Impedance responses of SOEC with SSC or $Ba_3(MnO_4)_2$-ATO anodes at (a) 700°C and (b) 600°C under various biases. 20%-H_2O/air was fed to the anode and 3%-H_2O/5%-H_2/Ar was fed to the cathode. In (a), S_h and S_l indicate the impedance arcs in high and low frequency ranges, respectively. The details are provided in the text

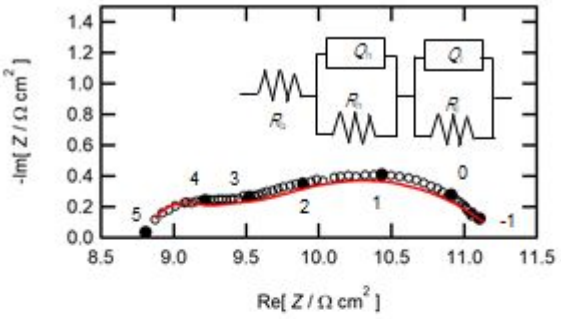

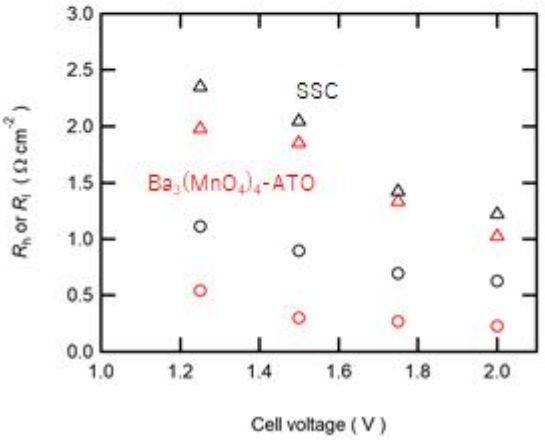

Figure 7 (a) Equivalent circuit fitting to the impedance spectra of SOEC with or $Ba_3(MnO_4)_2$-ATO anodes at 700 °C under 0.2 V cell voltage. Circles represent the measured data and solid line represents the fit with the model depicted in the inset. (b) R_h (circles) and R_l (triangles) of the impedance spectra of SOEC with SSC or $Ba_3(MnO_4)_2$-ATO anode under various DC conditions at 700 °C, which were determined by equivalent circuit analysis of the spectra displayed in Figure 6 (a).

Figure 8 Schemes for the anode reactions of H^+-SOEC with the reaction sites existing (a) over the electrode surface and (b) at the gas-electrode-electrolyte triple phase boundary. Impedance responses of SOEC with $Ba_3(MnO_4)_2$-ATO anodes, obtained by changing (c) p_{O2} and (e) p_{H2O} in the anode side at 700 °C. Circles are the observed values and solid lines are the fits obtained by equivalent circuit analysis with the model depicted in Fig. 7(a). Resultant R_h and R_l determined by equivalent circuit analysis of (d) p_{O2} and (f) p_{H2O}-variable impedance spectra